Research Article Vol. 1, No. 6 / December 2014 / Optica 446

Photonic generation of W-band arbitrary waveforms with high time-bandwidth products enabling 3.9 mm range resolution

Yihan Li,[1,†] Amir Rashidinejad,[1,†] Jhih-Min Wun,[2] Daniel E. Leaird,[1] Jin-Wei Shi,[2] and Andrew M. Weiner[1,*]

[1]School of Electrical and Computer Engineering, Purdue University, West Lafayette, Indiana 47907, USA

[2]Department of Electrical Engineering, National Central University, Jhongli 320, Taiwan

*Corresponding author: amw@purdue.edu

Received 27 August 2014; revised 5 November 2014; accepted 8 November 2014 (Doc. ID 221873); published 18 December 2014

Ultrabroadband millimeter-wave and subterahertz waveforms offer significant potential, from ultrahigh-speed communications to high-resolution radar. Electronic generation of broadband arbitrary waveforms at these frequencies suffers from limited digital-to-analog converter speed and high timing jitter. Photonic-assisted techniques, such as those based on optical shaping and frequency-to-time mapping, can overcome these difficulties. Nevertheless, previous photonic arbitrary waveform generation demonstrations are confined to microwave and low millimeter-wave frequencies due to limited optical-to-electrical conversion bandwidth. Here, by utilizing cutting-edge photodetector technology, we report the first generation, wireless transmission, and measurement of substantially complex and highly stable arbitrary waveforms in the W-band (75–110 GHz). These waveforms exhibit high time-bandwidth products up to 600, arbitrarily extendable repetition periods, and phase-noise performance substantially better than state-of-the-art electronic arbitrary waveform generators. The utility of the generated waveforms is demonstrated in multi-target ranging, where a depth resolution of 3.9 mm, unprecedented in the W-band, is achieved over more than 5 m.

OCIS codes: (060.5625) Radio frequency photonics; (320.5540) Pulse shaping; (230.5170) Photodiodes; (280.0280) Remote sensing and sensors.

http://dx.doi.org/10.1364/OPTICA.1.000446

1. INTRODUCTION

The last few decades have witnessed remarkable developments in millimeter-wave (MMW) and subterahertz (sub-THz) technology. High-frequency radio-frequency (RF) regions not only circumvent the extreme spectral congestion of lower RF bands, but also provide access to ultrabroad bandwidths for applications such as ultrahigh-speed wireless communication [1–6], high-resolution ranging [7–9], electromagnetic imaging and tomography [10–13], and high-speed spectroscopy [14–17]. A significant limitation in taking advantage of MMW and sub-THz technology has been the lack of versatile waveform generation in these regions. Due to the speed limitation of digital-to-analog converters (DACs), direct generation of arbitrary signals at frequencies in the range of 100 GHz and above is not a possibility using state-of-the-art electronics. Also, up-conversion [8,18,19] of electronically generated arbitrary baseband signals would still have bandwidth constraints—bounded by the intermediate frequency (IF) bandwidth of the mixer—and suffer severely from issues such as timing jitter, electromagnetic interference (EMI), and bulkiness [20,21]. These shortcomings have motivated researchers to pursue the possibility of photonic-assisted RF generation, which can provide not only broad bandwidths, but also exceptionally low timing jitter and phase-noise performance [22,23], immunity to EMI,

cost-effective and low propagation loss radio-over-fiber signal distribution, and the possibility of on-chip integration [20,21].

Recently, developments in robust optical arbitrary waveform generation (OAWG) techniques [24,25] have paved the way for versatile radio-frequency arbitrary waveform generation (RF-AWG) both at baseband frequencies [26–30] and at frequencies extending to the low MMW region [31,32]. Most of these schemes rely on optical pulse shaping [33] followed by frequency-to-time mapping (FTM) through chromatic dispersion to generate a wide variety of complex RF waveforms with instantaneous bandwidths well beyond electronics limits. While enjoying arbitrary programmability, until now, photonic-assisted RF-AWG methods have been confined to waveforms less than ~40 GHz [31,32], mainly limited by photodetector technology; hence experimental results in higher frequency bands are largely absent. One early experiment performed prior to the introduction of FTM used direct pulse shaping and a photoconductive dipole antenna to generate simply shaped THz bursts (ca. 1 THz center frequency), but with a very limited time-bandwidth product (TBP) [34]. In any case, although photonic approaches to arbitrary waveform generation offer large RF bandwidth, their repeatability, stability, frequency resolution, and jitter performance need further attention from the community.

In this paper, for the first time, to the best of our knowledge, we generate substantially complex and highly stable arbitrary waveforms in the 75–110 GHz range, termed W-band, showing how techniques developed at lower RF frequencies can be extended to much higher frequency ranges with advanced ultrahigh-speed photodetector technology [35–38]. Utilizing a specially engineered high-power near-ballistic uni-traveling-carrier photodiode (NBUTC-PD) [38] based photonic transmitter–mixer (PTM) [3,39], depicted in Fig. 1(a), we demonstrate the synthesis, wireless transmission, and detection of arbitrary RF waveforms in the W-band enabled by two different FTM-based photonic-assisted RF-AWG schemes. The passband RF-AWG method proposed in [32] is employed to generate, for the first time, to the best of our knowledge, ultrabroadband waveforms covering the whole W-band frequency region with a TBP of up to 600, the maximum supported by the pulse shaping element. Also, by switching between two anti-phase basis waveforms according to a predefined pseudorandom (PN) sequence, the time-aperture expansion technique described in [30] is applied to arbitrarily extend the repeat-free time aperture of the generated W-band waveforms, which in turn enhances the frequency resolution. The generated waveforms are further investigated in terms of repeatability and phase noise, demonstrating phase-noise characteristics substantially superior to those of a state-of-the-art electronic arbitrary waveform generator. Finally, as an application example, we demonstrate high-resolution ranging experiments that achieve range resolution down to 3.9 mm with the potential for an arbitrarily long unambiguous multi-target detection range, here demonstrated to over 5 m (10 m round-trip).

2. W-BAND EXPERIMENTAL CONFIGURATION

Figure 1(a) illustrates our W-band experimental arrangement. Optically tailored waveforms from the photonic RF-AWG setups are directed to the NBUTC-PD-based PTM [3,39]. Here, the adopted active NBUTC-PD with a 5 μm active

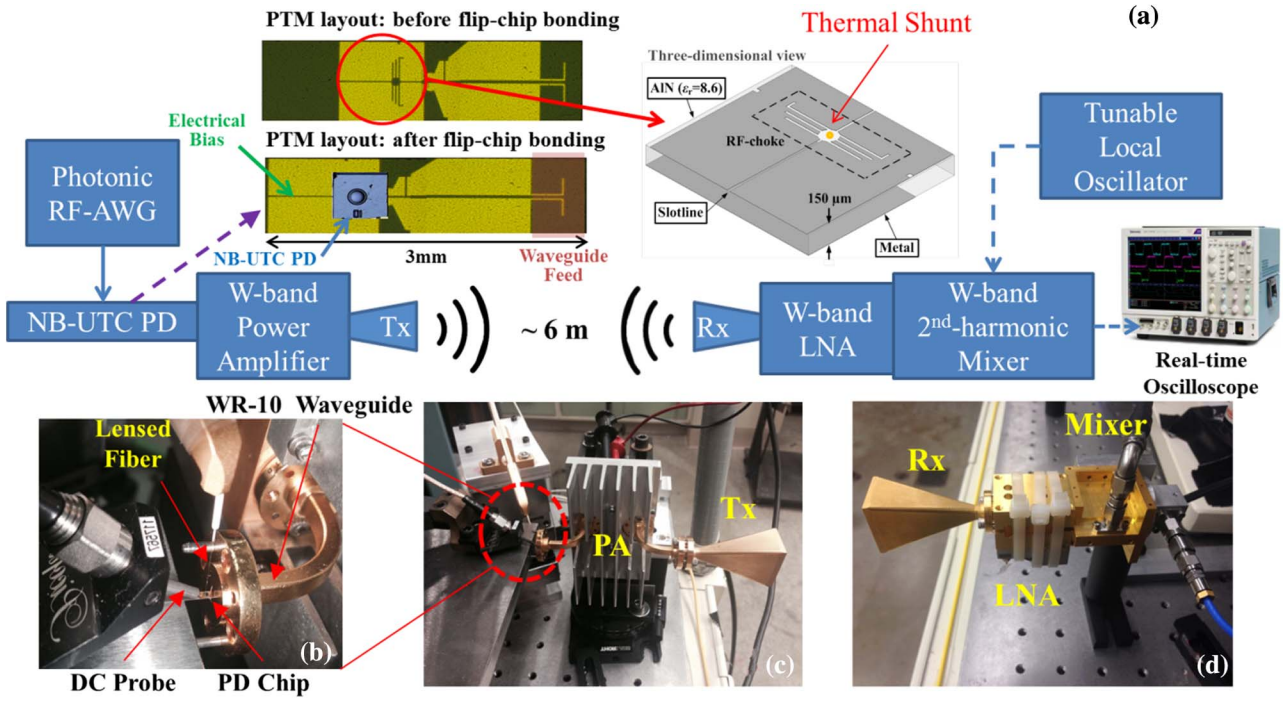

Fig. 1. W-band experimental setup. (a) Waveform generation, transmission, and measurement, including schematics of PTM chip before and after flip-chip bonding. NBUTC-PD, near-ballistic uni-traveling-carrier photodetector; Tx, transmitter antenna; Rx, receiver antenna; LNA, low-noise amplifier. (b) Close-up of O-E conversion block, followed by Tx feed. (c) Transmitter block. (d) Receiver block.

diameter has a >175 GHz optical-to-electrical (O-E) 3 dB bandwidth and the PTM package can cover the full W-band (75–110 GHz). The reference point for the bandwidth definition of PTM is according to its measured output power at the center of the W-band (~95 GHz). A detailed layout of the PTM package with AlN substrate for flip-chip bonding and WR-10 waveguide excitation is given in our previous work [3].

Compared with the NBUTC-PD structure reported in the previous works [3,38], the p-type $In_{0.53}Ga_{0.47}As$ absorption layer thickness has been increased from 160 to 260 nm. This leads to a significant improvement in DC responsivity from ~0.1 [3,38] to 0.25 A/W and saves the required optical power during high-output-power operation. In addition, the n-type InP collector layer thickness has been increased from 180 to 310 nm in order to relax the limitation on the maximum allowable device active diameter (>5 μm) for the desired RC-limited bandwidth (200 GHz). A larger device active diameter improves tolerance in optical alignment. However, the increased layer thickness leads to a reduction of the maximum output saturation current (power) of the PD, mainly due to the space charge screening effect [3,38]. A higher reverse bias voltage can be used to mitigate the space charge effect but introduces a junction temperature increase.

In order to alleviate this effect, as shown in Fig. 1(a), we insert a Au/Sn bump, 6 μm in diameter and 3 μm in height, as a thermal shunt on the layout of our PTM package. After flip-chip bonding, the thermal shunt is positioned within ~15 μm of the active PD mesa, improving device heat-sinking to the AlN substrate. The measured saturation current (power) of our PTM under −2 V bias, ~90% optical modulation depth, and 95 GHz operating frequency is ~18 mA (+2 dBm). These numbers are comparable with the reported values of the PTM without a thermal shunt [3] but with a thinner collector layer (180 versus 310 nm) in its active NBUTC-PD.

The overall apparatus along with photographs of the PTM chip, transmitter, and receiver are shown in Figs. 1(a)–1(d). The PTM is embedded in a WR-10 waveguide feed to excite a W-band power amplifier followed by a horn transmit antenna (Tx). At the receiver side, which is placed ~6 m away, a horn antenna (Rx), a W-band low-noise amplifier (LNA), and a subharmonic mixer (driven with frequencies from 35 to 50 GHz, ×2 multiplication factor to reach W-band) are used to collect, amplify, and downconvert the received waveforms. Details about the downconversion and measurement equipment are provided in the accompanying Supplement 1.

3. ULTRAHIGH TIME-BANDWIDTH PRODUCT RADIO-FREQUENCY ARBITRARY WAVEFORM

The schematic block diagram of this technique is depicted in Fig. 2(a). As introduced in [32], mode-locked (ML) laser pulse spectra are arbitrarily shaped through a stabilized interferometric shaping structure, in which one arm includes a high-resolution optical pulse shaper and the other a variable delay line (VDL). FTM is implemented via the introduction of a first-order chromatic dispersion (ψ_2 in units ps^2). In the far-field limit [40], the output optical waveform's intensity is simply a scaled replica of the shaped power spectrum. Thus,

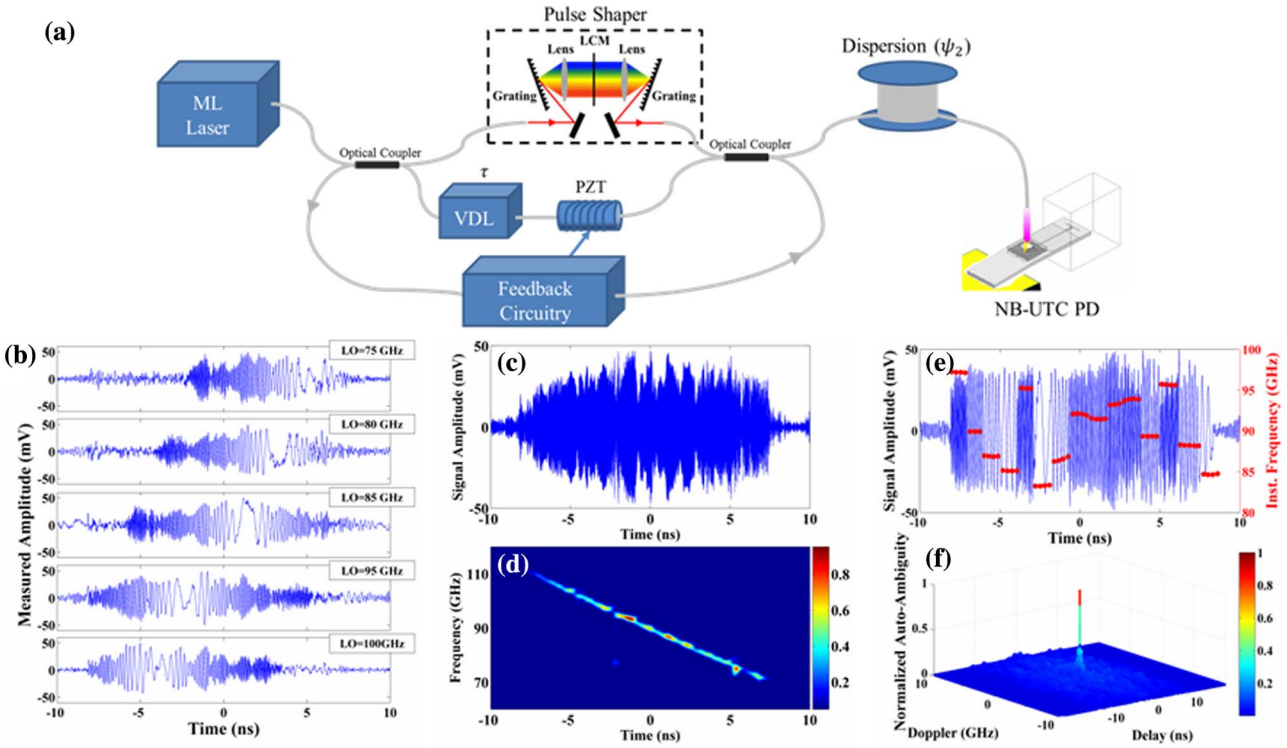

Fig. 2. Interferometric W-band RF-AWG. (a) Setup schematic. ML, mode-locked; VDL, variable delay line; PZT, piezo-electric transducer. (b) Down-converted measurements using various local oscillator (LO) frequencies. (c), (d) Reconstructed W-band waveform and spectrogram of ultrawideband linear down-chirp. (e) Reconstructed frequency-hopped Costas sequence (plotted in baseband) and corresponding instantaneous frequency. (f) Computed auto-ambiguity function of the waveform in (e).

through a simple photodetection stage, we can generate arbitrary RF waveforms described as follows:

$$i_{\mathrm{RF}}(t) \propto \left| H\left(\frac{t}{\psi_2}\right) \right| \cdot \cos\left(\frac{t\tau}{\psi_2} - \angle H\left(\frac{t}{\psi_2}\right) + \varphi_0\right). \quad (1)$$

Here, $i_{\mathrm{RF}}(t)$ is the bandpass photodetected current, $H(\omega) = |H(\omega)| \cdot \exp(j\angle H(\omega))$ is the pulse shaper's spectral transfer function, τ is the tunable interferometric delay, and $\varphi_0 = -\tau^2/2\psi_2$ is just a constant phase term.

Equation (1) demonstrates the ability of our scheme to generate arbitrary electrical waveforms by independently controlling the temporal amplitude, temporal phase, and center frequency (f_C) of $i_{\mathrm{RF}}(t)$ through the pulse shaper amplitude, the pulse shaper phase, and the variable delay, respectively. Moreover, the interferometric nature of the setup results in an intrinsically passband (e.g., 70–110 GHz) RF-AWG scheme, in contrast to the baseband nature (e.g., 0–110 GHz) of conventional [28] or near-field [31] FTM. As explained in [32], this permits us to attain the physical upper bound limit on TBP allowed by the pulse shaping device for generated waveforms in any specified frequency range, here W-band. With further advancements in high-resolution optical pulse shaping, such as geometries allowing access to high pixel counts, such as two-dimensional liquid crystal on silicon spatial light modulators [41], the TBP may be further extended, allowing the generation of even longer time durations for a fixed ultrabroad bandwidth.

Using this interferometric RF-AWG scheme in the configuration of Fig. 1(a), we program the pulse shaper to generate an ultrabroadband linear frequency-chirped electrical waveform from 110 GHz down to 70 GHz, encompassing the full W-band spectrum (more details provided in Supplement 1). Since the measurement apparatus only has ~17 GHz IF bandwidth (mainly limited by the mixing stage), the entire waveform cannot be measured at once. Consequently, different measurements of the same waveform using various local oscillator (LO) frequencies between 60 and 100 GHz are separately obtained, five of which are depicted in Fig. 2(b). These down-converted pulses each contain partial information about the generated signal and are the principal tools for reconstructing the complete W-band chirp.

Each LO measurement is digitally upconverted to its corresponding frequency, aligned in phase via offline processing, and combined with the other measurements to reconstruct the whole generated W-band linear down-chirp. It is important to note that the need for phase alignment results only from the lack of phase synchronism of the free-running LO that we tune to different frequencies and is not inherent to the generation scheme itself. The final reconstructed W-band chirp is illustrated in Fig. 2(c). The signal stretches over ~15 ns time aperture, consistent with the ~40 nm optical bandwidth and ~394 ps/nm dispersion. The slight amplitude fluctuations are mainly due to the spectral ripple in the optical domain, which in principle may be equalized using the pulse shaper's attenuation control. The spectrogram of the generated ultrawideband chirp is plotted in Fig. 2(d). Spectrograms are an example of a joint time–frequency distribution, an analysis tool used to characterize signals for which the frequency content is varying in time [42]. Here, the close-to-linear down-slope of the spectrogram clearly indicates the ability to achieve the target frequency chirp in the W-band, covering 70–110 GHz. As a result, a TBP of ~600 (40 GHz × 15 ns) is achieved in this experiment. Compared to previous demonstrations [19,43,44], to our knowledge this is the first experiment to achieve arbitrary waveforms with such high TBP values, while covering the full W-band spectrum. Also, as stated before, the interferometric shaping design allows us to reach the upper bound TBP, determined by the number of spectrally resolved control elements available from the optical pulse shaper (for more information, please refer to [32]).

The utilized scheme is not limited to chirp generation and can be reconfigured to attain truly arbitrary waveform generation. To demonstrate this capability, another interesting waveform, namely a wideband frequency-hopped Costas sequence [45] of length 15, is generated inside the W-band (more information in Supplement 1). Figure 2(e) illustrates the reconstructed temporal profile of this waveform (plotted after downconversion to baseband for clear observation of frequency transitions) alongside its instantaneous frequency. The center frequency is set to 90 GHz, and frequency steps occur in 1 GHz increments. Clear frequency transitions accompanied by a nearly flat temporal profile are observed. The waveform's auto-ambiguity function, which is a measure of a radar waveform's delay and Doppler sensitivity [45], is computed offline and plotted in Fig. 2(f). One of the desirable properties of Costas sequences is the sharp thumbtack shape of their auto-ambiguity function; this feature is clearly observed in Fig. 2(f). The main lobe of the auto-ambiguity has a full-width-half-maximum (FWHM) of 15 ps in delay and 36 MHz in Doppler. We note that the relatively coarse frequency resolution is a direct result of the short (nanosecond scale) time aperture of the generated pulses, limited in part by the repetition period (~18.9 ns) of the mode-locked laser at the front end, rendering it unsuitable for unambiguous long-range sensing and detection. However, by combining such photonic-assisted RF-AWG with a very simple modulation scheme, one may achieve much finer frequency resolution, with time aperture selectable up to microseconds and beyond, which accommodates practical applications. The details of this scheme are discussed in the following section.

4. ARBITRARILY LONG REPETITION PERIOD RADIO-FREQUENCY WAVEFORM GENERATION

Conventional ML-laser-based photonic RF-AWG techniques generate periodic waveforms with a fixed repetition rate equal to that of the mode-locked laser. This restriction severely limits the potential applications of the generated RF waveforms. For example, in ranging, having a short repetition period can lead to distance measurement ambiguities. Furthermore, as briefly pointed out above, frequency resolution lower than the laser repetition rate cannot be achieved. To overcome these hurdles and extend the repetition period of our waveforms arbitrarily, we implement the time-aperture expansion technique

explained in [30]. As sketched in Fig. 3(a), short optical pulses from a mode-locked laser are directed into either path where anti-phase spectral modulations are provided by two independent pulse shapers. After propagating through chromatic dispersion and impinging on the NBUTC-PD, the polarities of the generated pulses are oriented in an opposite fashion according to the switching pseudonoise (PN) sequence [45], resulting in an expanded repeat-free period and thus enhanced frequency resolution. The unambiguous sensing range can be set to microseconds or beyond simply by selecting long PN sequences under electronic control. Additionally, because only the polarity of the generated waveform is flipped, increases in peak-to-average power ratio are avoided, which is important in view of the peak-voltage-limited nature of most transmitters [30].

To demonstrate the repetition period expansion, we program the pulse shapers to generate linear frequency chirps covering 75–95 GHz with 2 ns time aperture. With the frequency of the LO set to 75 GHz, we measure the received waveforms over a 60 ns time range with and without length-15 PN switching. The waveforms recorded directly after downconversion are shown in Figs. 3(b) and 3(c). As explained previously, unmodulated chirps repeat themselves at the laser repetition period, here 4 ns (Fig. 3(b)); in contrast waveforms under PN switching exhibit pseudorandom polarity flipping, as highlighted by color coding in Fig. 3(c). These antipodal downconverted chirps are overlaid in the same plot in the inset between Figs. 3(b) and 3(c). For clear observation of the repetition period expansion, autocorrelation functions of both measurements are computed offline and plotted in Figs. 3(d) and 3(e).

In the absence of PN modulation, the autocorrelation, Fig. 3(d), is composed of compressed narrow peaks separated by 4 ns, the same as the laser repetition period, whereas the peak separation of the autocorrelation function for the PN-modulated sequence, Fig. 3(e), increases to 60 ns (15 × 4 ns), with all other 4-ns-spaced peaks suppressed by more than 13 dB. To demonstrate this technique even further, we increase the length of the modulation PN sequence to 1023, which results in a waveform with a more than 4 μm repetition period, as demonstrated via the autocorrelation plot of Fig. 3(f).

5. WAVEFORM GENERATION REPEATABILITY AND LOW-JITTER CHARACTERISTICS

From the application point of view, strong repeatability and low jitter are major requirements for the generated waveforms. For example, in pulse compression radar, repeatable generation of low-jitter sensing waveforms is a vital factor in achieving high-performance systems while maintaining low cost and complexity in the transceiver circuitry [46]. Several experiments have investigated the special case of photonic-assisted generation of MMW frequency-chirp waveforms, by beating a CW laser either with a second CW laser subject to rapid frequency tuning [43,44] or with a mode-locked pulse chirped under dispersive propagation [47]. However, the repeatability of the resulting waveforms is compromised, either due to the poor frequency sweep stability in the former case or due to phase drifts between the short pulse and CW lasers in the latter. Furthermore, phase-noise characteristics have not been

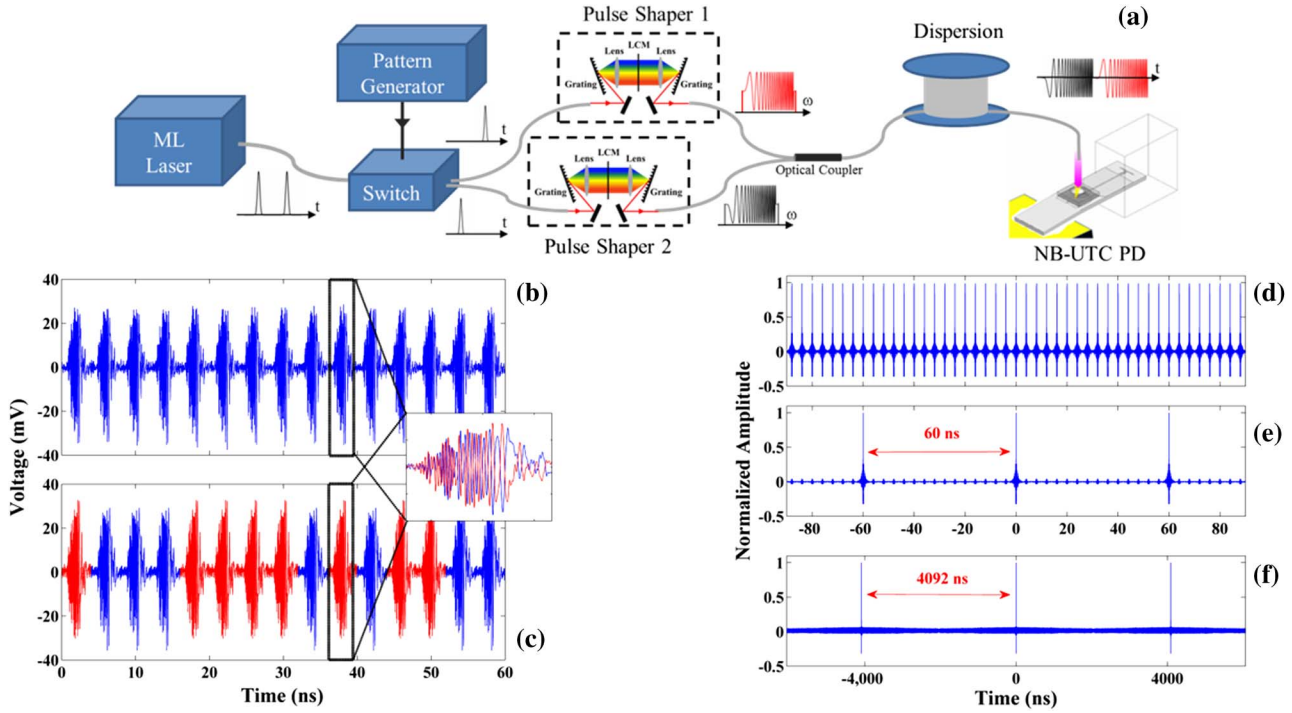

Fig. 3. Repetition period expanded W-band RF-AWG. (a) Setup schematic. (b) 60 ns measurement of downconverted W-band chirp pulse-train without PN modulation. (c) 60 ns measurement of downconverted W-band chirp pulse-train with length-15 PN modulation (red and blue indicating flipped polarity). (d) Autocorrelation of unmodulated waveforms. (e) Autocorrelation of length-15 PN modulated waveforms. (f) Autocorrelation of length-1023 PN modulated waveforms.

reported for either scheme. In contrast, our approach—presented for the W-band—benefits from both the excellent repeatability of FTM-based RF-AWG approaches [25,28] and the low-jitter potential of mode-locked laser sources [22,23].

To demonstrate this repeatability, we recorded a measurement of 4000 consecutive 2-ns-aperture down-chirp waveforms as per Fig. 3(b). The first down-chirp waveform is chosen as a reference, and we utilize cross correlations (without any offline phase alignment) with the reference to evaluate the similarity between these different down-chirp waveforms. These cross correlations are overlaid in the same temporal frame in Fig. 4 in blue. For comparison the autocorrelation of the reference is also computed and plotted in the same frame in red. Clearly, all 4000 correlations match each other very closely, providing compelling evidence of highly repeatable waveform generation.

Next, in order to evaluate phase noise, we program a single frequency tone at 80 GHz using the interferometric RF-AWG setup of Fig. 2(a), and after downconversion with a 78 GHz LO, perform single-sideband (SSB) phase-noise analysis using the phase-noise utility of our spectrum analyzer. Precise dispersion management (at the FTM stage) is carried out to line up consecutive pulses and achieve a quasi-continuous single frequency RF tone (details provided in Supplement 1). The blue curve in Fig. 5 plots the SSB phase noise of the generated (and downconverted) 80 GHz tone in the W-band. This phase-noise curve includes both the noise from the 80 GHz tone itself and the phase noise of the LO signal used in the downconversion stage. The phase noise of the 78 GHz LO signal is also plotted in the same figure in green. Specifically, as we observe from comparing these two curves, at frequency deviations above 10 kHz, phase noise is dominated by the LO signal, and not that of the W-band tone generated through our RF-AWG scheme. We also measure the phase noise of a 5 GHz continuous RF signal, generated with an electronic arbitrary waveform generator (Tektronix AWG 7000A, 9.6 GHz analog bandwidth at 6 dB), and project its phase noise—assuming ideal frequency multiplication—to 80 GHz (plotted in red). Here we assume that the phase noise scales as the multiplication factor squared [48], which gives a 24 dB increase for ideal ×16 multiplication. Note that this scaling factor is only a lower bound and does not account for any additional degradation that may occur in practical electronic or photonic-assisted [19] frequency multiplication. Furthermore, this scaling does not include any of the phase noise from the downconversion measurement to which the experimental optical phase curve is subject.

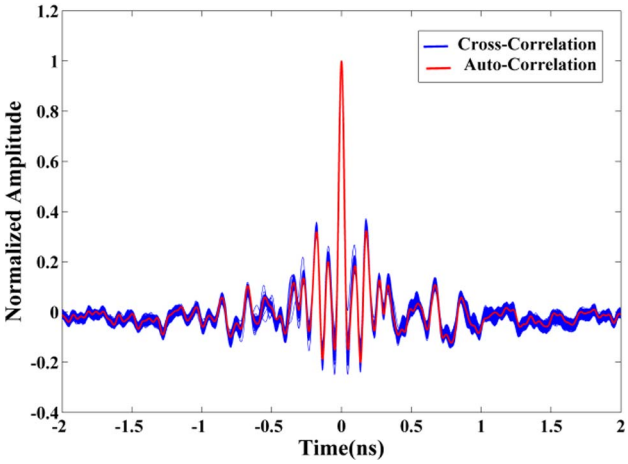

Fig. 4. Cross correlations between a reference chirped waveform and 4000 consecutive linear down-chirp waveforms (in blue) and autocorrelation of the reference down-chirp waveform (in red).

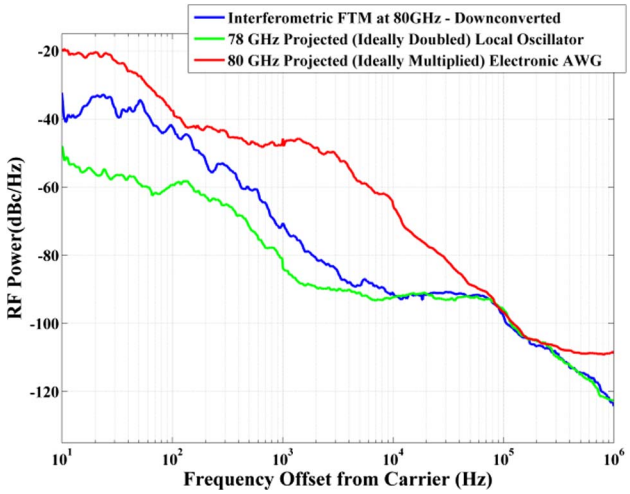

Fig. 5. Phase-noise comparison of 80 GHz continuous waveform (generated using photonic-assisted interferometric RF-AWG and downconverted with an LO at 2 × 39 GHz = 78 GHz), expected (projected) 78 GHz local oscillator phase-noise, and a 5 GHz signal from an electrical arbitrary waveform generator ideally multiplied to 80 GHz.

Figure 5 clearly shows that our scheme's phase noise for W-band generation substantially outperforms that projected for a frequency multiplied commercial electronic arbitrary waveform generator at all offset frequencies measured. According to the measurement, the phase-noise advantage of our scheme is as high as 35 dB (at ∼3.5 kHz offset).

Although the phase-noise advantages of mode-locked laser based generation of single frequency RF tones has been much explored [22,23], particularly around 10 GHz, the measurement presented here is the first to our knowledge confirming the potential for a strong phase-noise advantage in photonic arbitrary waveform generation. Given that our phase-noise measurement of the 80 GHz signal under photonic generation is limited by the LO over much of the range plotted, it is possible that the actual phase-noise advantage may be substantially better than suggested by Fig. 5. More advanced phase-noise measurement techniques, such as those utilized in work such as [22,23], would be beneficial in further exploring the phase-noise advantage obtainable with photonic-assisted RF-AWG.

6. RANGING: ARBITRARILY LONG-RANGE UNAMBIGUOUS DETECTION, ULTRAFINE RANGE RESOLUTION

As an application example we conduct a multi-target ranging experiment. The schematic block diagram of this setup is outlined in Fig. 6(a). Instead of directly facing each other,

the transmitter and receiver blocks in Fig. 1(a) are now positioned approximately side by side. Four reflective aluminum objects are placed within the antenna beams as targets. Ball A is located ~30 cm away from the transceiver. A double-plate set, consisting of two flat sheets B1 and B2, separated ~3 cm along the ranging direction, is placed ~3.8 m away from the antenna pair. A final reflector C is placed ~5.2 m away.

The 60-ns-long W-band sequences described in Figs. 3(b) and 3(c) are employed as sensing waveforms. After conducting the ranging procedure explained in Supplement 1, we obtain experimental results presented in Figs. 6(b) and 6(c). As demonstrated in Fig. 6(c), when PN-modulated chirps are transmitted, three main reflection peaks can be distinguished in the ranging result. The first peak, with roughly 0.2 normalized cross-correlation power, has a round-trip time of 2.114 ns, corresponding to a range displacement of 31.71 cm with respect to the transceiver. The relatively low peak height is due to the small radar cross section of the aluminum ball compared to the other objects. By magnification of the peak around ~25 ns (3.75 m) in Fig. 6(c), as shown in Fig. 6(d), we discover that it actually consists of two distinct peaks reflected from sheets B1 and B2. The 0.19 ns temporal difference between these two peaks indicates that the sheets are separated by 28.5 mm. Finally, there is a single peak from sheet C at 34.66 ns (5.2 m) with a lower peak height compared with those of the double-plate set because of more path loss through a longer propagation distance.

In contrast, when the unmodulated waveform is utilized, reflection peaks repeat themselves every 4 ns, the repetition period of the laser. Since the round-trip time span of these four objects is much longer (~35 ns), this creates ambiguity in determining the actual position of the reflectors [Fig. 6(b)]. Furthermore, we barely distinguish the reflection peak of the small metal sphere in Fig. 6(b) since it is submerged in the sidelobes of other stronger reflectors. These observations serve as convincing evidence that we are able to increase the unambiguous range of detection through our arbitrary expansion of the repetition period of the sensing waveform.

To demonstrate the range resolution of this setup, we gradually decrease the separation between the two flat sheets B1 and B2 and repeat the ranging procedure. The finest achieved depth resolution with a single setting of the LO is shown in Fig. 6(e). The two reflection peaks from the double-plate set are measured to be 50 ps apart, corresponding to a range resolution of 7.5 mm. Since the actual 3 dB RF bandwidth of the transmitted chirp waveform is degraded by the second-harmonic mixer to less than 17 GHz, a range resolution of 7.5 mm is approximately the theoretical limit attainable using such linear chirps [46].

By taking measurements with multiple LOs, we are able to circumvent the 17 GHz bandwidth limit of the mixer and achieve even finer resolution. The setup is similar to that of Fig. 6(a). However, since we are emphasizing resolution, we use only targets B1 and B2. We program a linear down-chirp

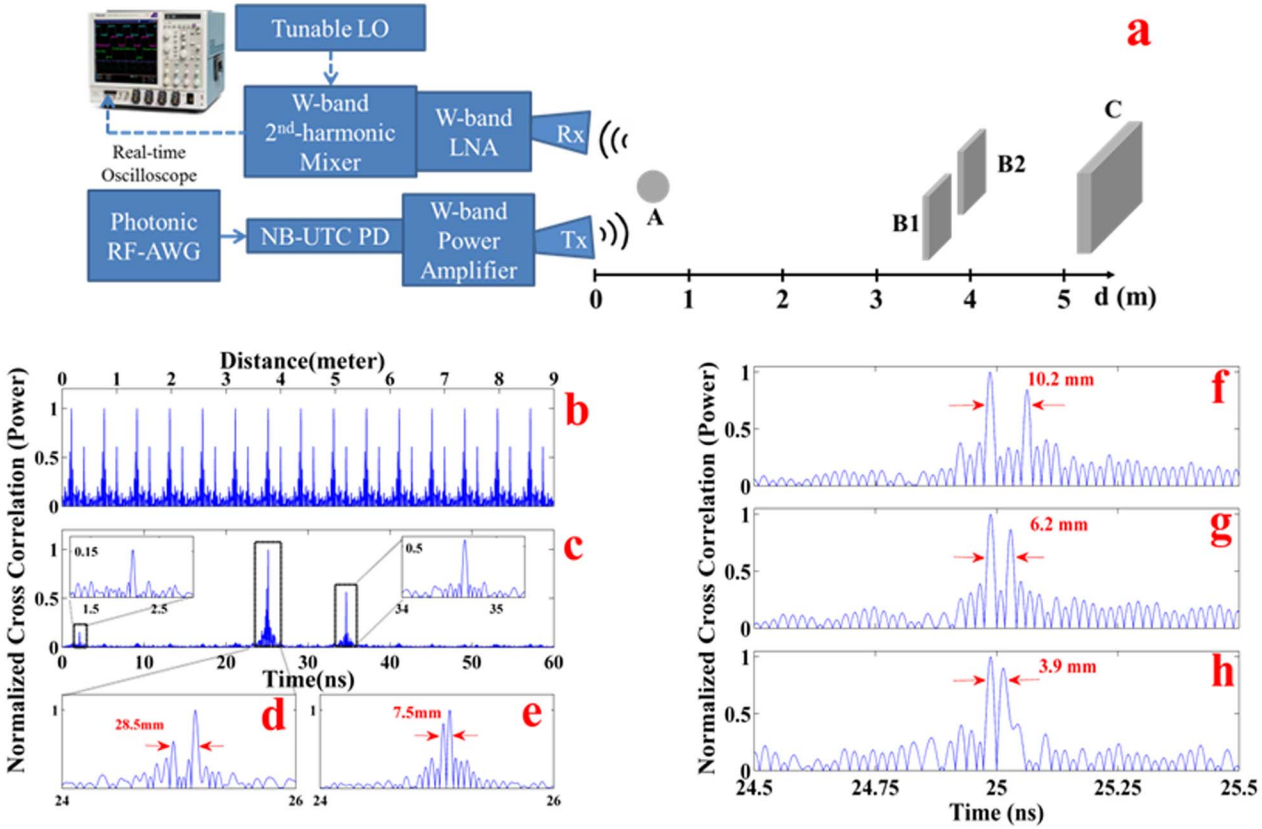

Fig. 6. Ultrahigh-resolution W-band ranging experiments. (a) Setup schematic. Ball A with radius 4 cm. Flat sheets B1 and B2 are 10 × 10 cm. Flat sheet C is 10 × 15 cm. (b) Long-range W-band ranging with unmodulated sensing waveforms. (c) Long-range W-band ranging with length-15 PN-modulated sensing waveforms. (d) Magnified view from 24–26 ns of (c). (e) Achieved finest range resolution (single measurement). (f)–(h) Ultrafine W-band ranging experimental results with ~10, ~6, and ~4 mm target separation (multiple measurements).

Table 1. Comparison of Prominent MMW and Sub-THz Ranging System

RF Ranging System	Center Frequency (GHz)	Bandwidth (GHz)	Sensing Waveform	Range Resolution (cm)
Ref. [9]	94	12	Short pulse	1.2
Ref. [49]	95	0.84	Linear chirp	30
Ref. [50]	94	0.8	FMCW[a]	19
Ref. [7]	590	29	FMCW	0.5
Ref. [8]	675	26	FMCW	0.58
This work	85	30	Linear chirp	0.39

[a]FMCW: Frequency-modulated continuous-wave radar.

from 70 to 100 GHz employing the interferometric RF-AWG scheme (Fig. 2), and take two measurements, with LO frequencies of 70 and 100 GHz, respectively, for various spacings between the two objects. We first place the two reflectors roughly 10 mm from each other and retrieve their relative distance via cross correlation. The cross-correlation plot is depicted in Fig. 6(f). The time difference between the two peaks yields a 10.2 mm distance between the two objects. Next we move the objects closer to each other and generate new cross correlations. The results of placing the objects at ~6 and ~4 mm are illustrated in Figs. 6(g) and 6(h). In each case the cross-correlation peak pairs are clearly distinct and differentiable from the background noise and sidelobes. Figure 6(h) depicts the finest depth resolution we experimentally obtained. The 3.9 mm separation is very close to the theoretical limit for a 30 GHz ranging chirp.

To our knowledge, the achieved 3.9 mm range resolution is significantly better than previous demonstrations in the W-band [9,49,50], including both electrical and photonic-assisted schemes. It also improves, but to a lesser extent, on resolutions reported for experiments with signals generated electronically in considerably higher MMW and sub-THz frequency bands [7,8]. By generating sensing waveforms with comparable bandwidths but at substantially lower center frequencies (~90 GHz as compared with ~600 GHz), we provide a practical way to overcome the excessive path loss and atmospheric absorption of the higher frequency regions, without sacrificing range resolution, while still avoiding the congestion in the microwave and low MMW regime. A further comparison of our scheme with previous works is provided in Table 1. We must also point out that the arbitrariness of our generated waveforms can provide added opportunities for optimization of the sensing waveform, such as windowing for sidelobe suppression and Doppler-immune radar [45,46].

7. SUMMARY

With the help of a high-performance NBUTC-PD-based photonic mixer module, we report photonic-assisted generation of RF arbitrary waveforms in the 70–110 GHz W-band frequency region. These waveforms can span the full W-band with the maximum TBP supported by the optical pulse shaper, highly attractive phase-noise characteristics, arbitrarily long repetition period, and high stability. With appropriate photodetector and antenna technologies, it should be possible to extend these techniques to even higher frequency regions. As an application example, we utilize the tailored W-band signals in ranging experiments, demonstrating both ultrafine depth resolution (down to 3.9 mm) and unambiguous detection over a range of more than 5 m. These results can be significantly enhanced by increasing the bandwidth of the measurement block and lengthening the PN modulation sequence. Our work features reconfigurable low-jitter waveform generation with instantaneous RF bandwidth unprecedented in this frequency range and offers potential for new horizons in high-resolution ranging, high-speed wireless communication, electromagnetic imaging and tomography, and high-speed spectroscopy.

[†]These authors contributed equally to this work.

FUNDING INFORMATION

Agilent Technologies (Research Grant 3230); National Science Council Taiwan (NSC) (101-2221-E-007-103-MY3); National Science Foundation (NSF) (ECCS-1126314); Naval Postgraduate School, Office of the Secretary of Defense and Engineering (N00244-09-1-0068); US Asian Office of Aerospace Research and Development (AOARD-13-4088).

See Supplement 1 for supporting content.

REFERENCES

1. J. Federici and L. Moeller, "Review of terahertz and subterahertz wireless communications," J. Appl. Phys. **107**, 111101 (2010).
2. J. W. Shi, C. B. Huang, and C. L. Pan, "Millimeter-wave photonic wireless links for very high data rate communication," NPG Asia Mater. **3**, 41–48 (2011).
3. N. W. Chen, J. W. Shi, H. J. Tsai, J. M. Wun, F. M. Kuo, J. Hesler, T. W. Crowe, and J. E. Bowers, "Design and demonstration of ultrafast W-band photonic transmitter-mixer and detectors for 25 Gbits/sec error-free wireless linking," Opt. Express **20**, 21223–21234 (2012).
4. X. Y. Li, Z. Dong, J. J. Yu, N. Chi, Y. F. Shao, and G. K. Chang, "Fiber-wireless transmission system of 108 Gb/s data over 80 km fiber and 2 × 2 multiple-input multiple-output wireless links at 100 GHz W-band frequency," Opt. Lett. **37**, 5106–5108 (2012).
5. S. Koenig, D. Lopez-Diaz, J. Antes, F. Boes, R. Henneberger, A. Leuther, A. Tessmann, R. Schmogrow, D. Hillerkuss, R. Palmer, T. Zwick, C. Koos, W. Freude, O. Ambacher, J. Leuthold, and I. Kallfass, "Wireless sub-THz communication system with high data rate," Nat. Photonics **7**, 977–981 (2013).
6. T. Nagatsuma, S. Horiguchi, Y. Minamikata, Y. Yoshimizu, S. Hisatake, S. Kuwano, N. Yoshimoto, J. Terada, and H. Takahashi, "Terahertz wireless communications based on photonics technologies," Opt. Express **21**, 23736–23747 (2013).
7. K. B. Cooper, R. J. Dengler, N. Llombart, T. Bryllert, G. Chattopadhyay, E. Schlecht, J. Gill, C. Lee, A. Skalare, I. Mehdi, and P. H. Siegel, "Penetrating 3-D imaging at 4-and 25-m range using a submillimeter-wave radar," IEEE Trans. Microwave Theor. Tech. **56**, 2771–2778 (2008).
8. K. B. Cooper, R. J. Dengler, N. Llombart, A. Talukder, A. V. Panangadan, C. S. Peay, I. Mehdia, and P. H. Siegel, "Fast, high-resolution terahertz radar imaging at 25 meters," Proc. SPIE **7671**, 76710Y (2010).
9. T. F. Tseng, J. M. Wun, W. Chen, S. W. Peng, J. W. Shi, and C. K. Sun, "High-depth-resolution 3-dimensional radar-imaging system based on a few-cycle W-band photonic millimeter-wave pulse generator," Opt. Express **21**, 14109–14119 (2013).

10. R. W. McMillan, "Terahertz imaging, millimeter-wave radar," in *Advances in Sensing with Security Applications*, Vol. **2** of NATO Security through Science Series (Springer, 2006), pp. 243–268.
11. M. Tonouchi, "Cutting-edge terahertz technology," Nat. Photonics **1**, 97–105 (2007).
12. J. A. Zeitler and L. F. Gladden, "In-vitro tomography and non-destructive imaging at depth of pharmaceutical solid dosage forms," Eur. J. Pharmaceutics Biopharmaceutics **71**, 2–22 (2009).
13. D. M. Sheen, J. L. Fernandes, J. R. Tedeschi, D. L. McMakin, A. M. Jones, W. M. Lechelt, and R. H. Severtsen, "Wide-bandwidth, wide-beamwidth, high-resolution, millimeter-wave imaging for concealed weapon detection," Proc. SPIE **8715**, 871509 (2013).
14. H. J. Hansen, "Standoff detection using millimeter and submillimeter wave spectroscopy," Proc. IEEE **95**, 1691–1704 (2007).
15. L. Chao, M. N. Afsar, and K. A. Korolev, "Millimeter wave dielectric spectroscopy and breast cancer imaging," in *7th European Microwave Integrated Circuits Conference* (IEEE, 2012), pp. 572–575.
16. J. L. Neill, B. J. Harris, A. L. Steber, K. O. Douglass, D. F. Plusquellic, and B. H. Pate, "Segmented chirped-pulse Fourier transform submillimeter spectroscopy for broadband gas analysis," Opt. Express **21**, 19743–19749 (2013).
17. A. P. Colombo, Y. Zhou, K. Prozument, S. L. Coy, and R. W. Field, "Chirped-pulse millimeter-wave spectroscopy: spectrum, dynamics, and manipulation of Rydberg-Rydberg transitions," J. Chem. Phys. **138**, 014301 (2013).
18. L. A. Samoska, "An overview of solid-state integrated circuit amplifiers in the submillimeter-wave and THz regime," IEEE Trans. Terahertz Sci. Technol. **1**, 9–24 (2011).
19. A. Kanno and T. Kawanishi, "Broadband frequency-modulated continuous-wave signal generation by optical modulation technique," J. Lightwave Technol. **32**, 3566–3572 (2014).
20. A. J. Seeds and K. J. Williams, "Microwave photonics," J. Lightwave Technol. **24**, 4628–4641 (2006).
21. J. Capmany and D. Novak, "Microwave photonics combines two worlds," Nat. Photonics **1**, 319–330 (2007).
22. F. Quinlan, T. M. Fortier, H. Jiang, A. Hati, C. Nelson, Y. Fu, J. C. Campbell, and S. A. Diddams, "Exploiting shot noise correlations in the photodetection of ultrashort optical pulse trains," Nat. Photonics **7**, 290–293 (2013).
23. T. M. Fortier, M. S. Kirchner, F. Quinlan, J. Taylor, J. C. Bergquist, T. Rosenband, N. Lemke, A. Ludlow, Y. Jiang, C. W. Oates, and S. A. Diddams, "Generation of ultrastable microwaves via optical frequency division," Nat. Photonics **5**, 425–429 (2011).
24. Z. Jiang, C. B. Huang, D. E. Leaird, and A. M. Weiner, "Optical arbitrary waveform processing of more than 100 spectral comb lines," Nat. Photonics **1**, 463–467 (2007).
25. S. T. Cundiff and A. M. Weiner, "Optical arbitrary waveform generation," Nat. Photonics **4**, 760–766 (2010).
26. J. D. McKinney, D. E. Leaird, and A. M. Weiner, "Millimeter-wave arbitrary waveform generation with a direct space-to-time pulse shaper," Opt. Lett. **27**, 1345–1347 (2002).
27. J. Chou, Y. Han, and B. Jalali, "Adaptive RF-photonic arbitrary waveform generator," IEICE Trans. Electron. **E86C**, 1226–1229 (2003).
28. I. S. Lin, J. D. McKinney, and A. M. Weiner, "Photonic synthesis of broadband microwave arbitrary waveforms applicable to ultra-wideband communication," IEEE Microwave Wirel. Compon. Lett. **15**, 226–228 (2005).
29. M. H. Khan, H. Shen, Y. Xuan, L. Zhao, S. J. Xiao, D. E. Leaird, A. M. Weiner, and M. H. Qi, "Ultrabroad-bandwidth arbitrary radiofrequency waveform generation with a silicon photonic chip-based spectral shaper," Nat. Photonics **4**, 117–122 (2010).
30. Y. Li, A. Dezfooliyan, and A. M. Weiner, "Photonic synthesis of spread spectrum radio frequency waveforms with arbitrarily long time apertures," J. Lightwave Technol. **32**, 3580–3587 (2014).
31. A. Dezfooliyan and A. M. Weiner, "Photonic synthesis of high fidelity microwave arbitrary waveforms using near field frequency to time mapping," Opt. Express **21**, 22974–22987 (2013).
32. A. Rashidinejad and A. M. Weiner, "Photonic radio-frequency arbitrary waveform generation with maximal time-bandwidth product capability," J. Lightwave Technol. **32**, 3383–3393 (2014).
33. A. M. Weiner, "Ultrafast optical pulse shaping: a tutorial review," Opt. Commun. **284**, 3669–3692 (2011).
34. Y. Q. Liu, S. G. Park, and A. M. Weiner, "Enhancement of narrow-band terahertz radiation from photoconducting antennas by optical pulse shaping," Opt. Lett. **21**, 1762–1764 (1996).
35. H. Ito, S. Kodama, Y. Muramoto, T. Furuta, T. Nagatsuma, and T. Ishibashi, "High-speed and high-output InP-InGaAs unitraveling-carrier photodiodes," IEEE J. Sel. Top. Quantum Electron. **10**, 709–727 (2004).
36. A. Beling, H. G. Bach, G. G. Mekonnen, R. Kunkel, and D. Schmidt, "High-speed miniaturized photodiode and parallel-fed traveling-wave photodetectors based on InP," IEEE J. Sel. Top. Quantum Electron. **13**, 15–21 (2007).
37. A. Stohr, S. Babiel, P. J. Cannard, B. Charbonnier, F. van Dijk, S. Fedderwitz, D. Moodie, L. Pavlovic, L. Ponnampalam, C. C. Renaud, D. Rogers, V. Rymanov, A. Seeds, A. G. Steffan, A. Umbach, and M. Weiss, "Millimeter-wave photonic components for broadband wireless systems," IEEE Trans. Microwave Theor. Tech. **58**, 3071–3082 (2010).
38. J. W. Shi, F. M. Kuo, and J. E. Bowers, "Design and analysis of ultra-high-speed near-ballistic uni-traveling-carrier photodiodes under a 50-omega load for high-power performance," IEEE Photon. Technol. Lett. **24**, 533–535 (2012).
39. N.-W. Chen, H.-J. Tsai, F.-M. Kuo, and J.-W. Shi, "High-speed-band integrated photonic transmitter for radio-over-fiber applications," IEEE Trans. Microwave Theor. Tech. **59**, 978–986 (2011).
40. V. Torres-Company, D. E. Leaird, and A. M. Weiner, "Dispersion requirements in coherent frequency-to-time mapping," Opt. Express **19**, 24718–24729 (2011).
41. A. M. Metcalf, V. Torres-Company, V. Supradeepa, D. E. Leaird, and A. M. Weiner, "Fully programmable two-dimensional pulse shaper for broadband line-by-line amplitude and phase control," Opt. Express **21**, 28029–28039 (2013).
42. L. Cohen, "Time-frequency distributions—a review," Proc. IEEE **77**, 941–981 (1989).
43. J. W. Shi, F. M. Kuo, N. W. Chen, S. Y. Set, C. B. Huang, and J. E. Bowers, "Photonic generation and wireless transmission of linearly/nonlinearly continuously tunable chirped millimeter-wave waveforms with high time-bandwidth product at W-band," IEEE Photon. J. **4**, 215–223 (2012).
44. J. M. Wun, C. C. Wei, J. H. Chen, C. S. Goh, S. Y. Set, and J. W. Shi, "Photonic chirped radio-frequency generator with ultra-fast sweeping rate and ultra-wide sweeping range," Opt. Express **21**, 11475–11481 (2013).
45. N. Levanon and E. Mozeson, *Radar Signals* (Wiley, 2004).
46. N. Levanon, *Radar Principles* (Wiley-Interscience, 1988).
47. H. B. Gao, C. Lei, M. H. Chen, F. J. Xing, H. W. Chen, and S. Z. Xie, "A simple photonic generation of linearly chirped microwave pulse with large time-bandwidth product and high compression ratio," Opt. Express **21**, 23107–23115 (2013).
48. E. Rubiola, *Phase Noise and Frequency Stability in Oscillators*, The Cambridge RF and Microwave Engineering Series (Cambridge University, 2009).
49. A. Y. Nashashibi, K. Sarabandi, P. Frantzis, R. D. De Roo, and F. T. Ulaby, "An ultrafast wide-band millimeter-wave (MMW) polarimetric radar for remote sensing applications," IEEE Trans. Geosci. Remote Sens. **40**, 1777–1786 (2002).
50. H. Essen, M. Hägelen, A. Wahlen, K. Schulz, K. Jäger, and M. Hebel, "ISAR imaging of helicopters using millimeter wave radars," Int. J. Microwave Wireless Technol. **1**, 171–178 (2009).